Journal of Catalysis 426 (2023) 294–300

Contents lists available at ScienceDirect

Journal of Catalysis

journal homepage: www.elsevier.com/locate/jcat

Destruction and preservation of nonstoichiometric ZnCr oxide catalyst from machine-learning simulation

Sicong Ma [a], Cheng Shang [b], Zhi-Pan Liu [a,b,c,*]

[a] Key Laboratory of Synthetic and Self-Assembly Chemistry for Organic Functional Molecules, Shanghai Institute of Organic Chemistry, Chinese Academy of Sciences, Shanghai 200032, China

[b] Shanghai Key Laboratory of Molecular Catalysis and Innovative Materials, Key Laboratory of Computational Physical Science, Department of Chemistry, Fudan University, Shanghai 200433, China

[c] Shanghai Qi Zhi Institution, Shanghai 200030, China

ARTICLE INFO

Keywords:
Solid disproportionation reaction
Zn-Cr Oxide
Neural network
Molecular dynamic
Al-doping

ABSTRACT

Structural destruction, for example via the solid disproportionation reaction (SDR), is one of the main causes of catalyst deactivation that often lacks atomic level understanding due to the strong coupling of reaction conditions and the long-time scale of the structural evolution. Here by using machine-learning-based atomic simulations we are able to clarify the detailed deactivation mechanism of the nonstoichiometric zinc-chromium oxide ($ZnCr_xO_y$) catalyst, an important industrial catalyst for syngas conversion. We show that the reductive reaction conditions first lead to the generation of surface and subsurface oxygen vacancies, and the subsequent cation migration via the replacement of subsurface Zn by surface Cr kills the catalyst activity by diminishing the active surface planer [CrO_4] sites. The rate-determining step, the Zn/Cr cation migration, is exothermic towards forming stoichiometric $ZnCr_2O_4$, and has an accessible barrier (~1.7 eV) under syngas conversion reaction conditions, indicating that the long-term deactivation is inevitable. By screening a set of additive elements, we demonstrate that Al element is an effective inhibitor to impede the formation of subsurface oxygen vacancy, the initial step of SDR. Our findings demonstrate the power of machine-learning-based atomic simulations in elucidating complex structural transformations and provide directions to mitigate $ZnCr_xO_y$ catalyst deactivation.

1. Introduction

Catalyst durability under harsh reaction conditions is a key concern in industrial applications. Zinc-chromium oxide ($ZnCr_xO_y$) catalyst, the first-generation industrial catalyst for syngas-to-methanol conversion [1–2], was renowned for the high-temperature deactivation problem in a long-term operation, which limits its large-scale applications, in particular for the recently identified catalytic syngas-to-olefin conversion when $ZnCr_xO_y$ is used in combination with zeolite working above 600 K [3]. In general, the catalyst with a nonstoichiometric Zn:Cr ratio of 1:1 is the most active composition, which undergoes severe deactivation, e.g. from 80 wt% to 60 wt% for syngas-to-alcohol selectivity after 1000 h [4]. The increase of the reaction temperature aggravates the deactivation, e.g. from 392 g $kg_{cat}^{-1}h^{-1}$ at 623 K to 194 g $kg_{cat}^{-1}h^{-1}$ at 673 for methanol yield [5]. It is of great significance to understand the deactivation mechanism and find measures to prevent the catalyst degradation.

The active $ZnCr_xO_y$ catalysts generally have a face-centered cubic sublattice formed by O^{2-} anions, the characteristics of spinel phase, but with different Zn and Cr occupations in the interstitial tetrahedral and octahedral sites. The least active phase, a stoichiometric $ZnCr_2O_4$ spinel crystal, is the most stable phase as it forms after high-temperature calcination, where Zn^{2+} and Cr^{3+} cations are located in tetrahedral and octahedral sites ([ZnO_4] and [CrO_6]), respectively. With Zn:Cr ratio larger than 1:2, there are a series of nonstoichiometric Z $ZnCr_xO_y$ spinel phases identified from Zn-Cr-O three phase diagram, including the metastable $Zn_5Cr_7O_{16}$, $Zn_3Cr_3O_8$ phases, etc. [6]. These nonstoichiometric $ZnCr_xO_y$ spinel phases contain the special [ZnO_6] structural pattern (Zn at octahedral site) [5–12].

By characterizing the structure of $ZnCr_xO_y$ catalyst, it was shown that the coordination environments of cations change dramatically during reaction. The X-ray absorption near edge structure (XANES) spectra

---

* Corresponding author at: Key Laboratory of Synthetic and Self-Assembly Chemistry for Organic Functional Molecules, Shanghai Institute of Organic Chemistry, Chinese Academy of Sciences, Shanghai 200032, China.

E-mail address: zpliu@fudan.edu.cn (Z.-P. Liu).

https://doi.org/10.1016/j.jcat.2023.07.024
Received 24 April 2023; Received in revised form 6 July 2023; Accepted 26 July 2023
Available online 29 July 2023

show that the fresh and used $ZnCr_xO_y$ catalysts after 1000 h reaction differ obviously in the intensity at two peaks, i.e. peak **A** at 9665 ~ 9675 eV and peak **B** at 9678 ~ 9685 eV (Fig. 1a). The shift to high energy and decrease of **A** and increase of **B** are attributed to the redistribution of bulk Zn from octahedral to tetrahedral sites.[4] In addition, the X-ray diffraction (XRD) shows that the lattice parameter of the spinel phase decreases from 8.36 Å to 8.32 Å ($ZnCr_2O_4$) and a ZnO peak emerges and grows over reaction time [5,9,13]. It was therefore proposed that the deactivation of $ZnCr_xO_y$ catalyst (Zn:Cr $>$ 1:2) is caused by solid disproportionation reaction (SDR), where the less stable non-stoichiometric $ZnCr_xO_y$ spinel phase ejects ZnO to form the stoichiometric $ZnCr_2O_4$ phase, following the reaction formula: $ZnCr_xO_y$-> $ZnCr_2O_4$ + ZnO [5,7–10].

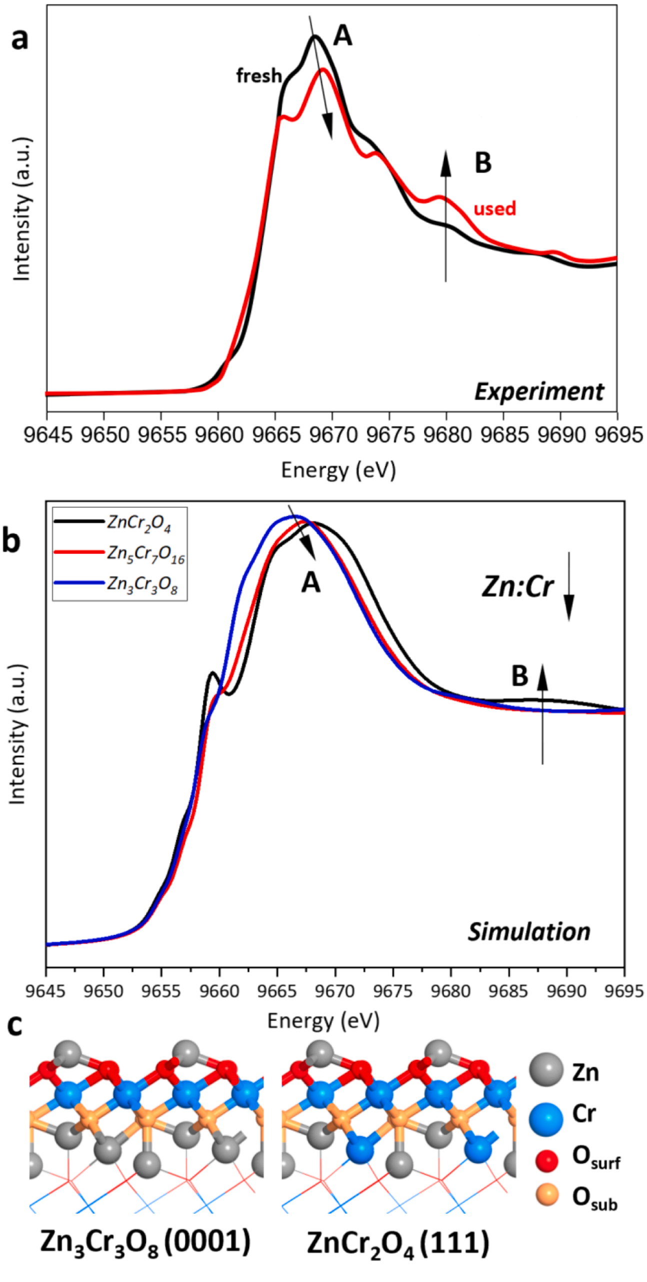

Fig. 1. (a) The experiment and (b) simulated Zn K-edge XANES spectra of $ZnCr_xO_y$ catalyst. The experimental data of XANES spectrum is from reference 4. (c) The structure of the $Zn_3Cr_3O_8$ (0001) and $ZnCr_2O_4$ (1 1 1), the most stable surfaces of the nonstoichiometric $Zn_3Cr_3O_8$ and stoichiometric $ZnCr_2O_4$. The gray, light blue and red/orange represent the Zn, Cr and surface/subsurface O atoms, respectively.

In fact, SDR is a special solid phase transition with important industrial application for the production of cement and catalyst synthesis. By definition, in SDR a single solid compound undergoes the atomic rearrangement and decomposition, resulting in the formation of two or more different compounds. For $ZnCr_xO_y$ SDR, it involves a number of reaction events, including the disappearance of [ZnO_6], the regeneration of [CrO_6] and the agglomeration of Zn element, where the slip and deformation of structural units must occur in accompanied with the atom long-distance migration [14–15]. Due to the complexity of SDR, the atomic-level understanding of the SDR process is difficult to achieve from experiment and no detailed mechanism is now available to rationalize the deactivation process for $ZnCr_xO_y$, not even mentioning to rationally prevent the catalyst deactivation.

On the other hand, the theoretical simulations have been widely practiced in modeling catalyst structures and predicting the catalytic activity. The atomic simulations based on density functional theory (DFT), although being available in the 1960 s, fails to explore the phase space of complex SDR owing to its high computational cost. As practiced by our group in recent years [6,16–17], the large-scale atomic simulations of complex materials are now feasible with the advent of global neural network (G-NN) potential, which achieves several orders of magnitude ($>10^4$) speed-up at the similar accuracy compared to DFT calculations.

Here by combining a state-of-art G-NN potential and efficient potential energy surface (PES) exploration methods, we are able to reveal the mechanism of $ZnCr_xO_y$ SDR by examining the vast structural space and identifying the lowest energy evolution process of $ZnCr_xO_y$. The key events in SDR are identified: the oxygen anion migration to form subsurface oxygen vacancy and the Zn/Cr cation exchange with the subsurface Zn replaced by the surface Cr. We further show that the Al element is a good additive to slow down the SDR rate.

2. Computational details

Our approach for resolving complex oxide structures is based on the G-NN-based PES explorations methods as implemented in LASP code [18], which shows the great potential to resolve the complex catalyst structure in heterogeneous catalysis [16]. In particular, the stochastic surface walking (SSW) algorithm, an unbiased global optimization method, is utilized for global structure search and pathway sampling [19], and the molecular dynamics (MD) simulation is used to obtain the high-temperature long-time trajectory of anion and cation migrations.

The machine learning G-NN potential is generated by iterative self-learning of the plane wave DFT global dataset generated from global PES exploration. More details about the construction of G-NN potential can be found in our previous work.[6] The final energy and force criteria of the root mean square errors for Zn-Cr-O (Zn-Cr-Al-O) NN potentials were around 4.3 (6.2) meV/atom and 0.13 (0.15) eV/Å respectively. DFT calculations are utilized to validate the low energy structures to confirm the identified global minimum and all energetics reported here are from DFT without specifically mentioning. The MD-NN simulation is performed on the canonical ensemble (NVT) at different temperatures. The MD simulation runs for at least 2 ns with the time step of 1 fs.

The DFT calculations utilized to generate the global dataset and validate the reaction profiles are performed by using plane wave DFT code, VASP, where electron–ion interaction is represented by the projector augmented wave (PAW) pseudopotential [20–21]. The exchange–correlation functional utilized is the GGA-PBE [22] with Hubbard-like term (U_{eff}) correction describing the on-site Coulombic interaction. The U_{eff} value for the Cr *3d* orbital is 3.3 eV [6]. The valence electrons were expanded in a plane-wave basis set within a cutoff energy of 400 eV. The first Brillion zone k-point sampling utilizes an automated Monkhorst-Pack scheme with the mesh determined by 18 times of the reciprocal lattice vectors (18 $Å^{-1}$). The energy and force criterions for convergence of the electron density and structure optimization were set at 10^{-6} eV and 0.02 eV/Å, respectively. Transition states (TSs) for all the elementary reactions were located using the efficient double-ended surface walking (DESW) method [23–24].

To determine the O_v formation energy, *ab initio* thermodynamics analyses are performed with equation (1) to compute the Gibbs free energy change (ΔG_{Ov}) under the reaction conditions (H_2 at 673 K and 2.5 MPa syngas pressure):

$$ZnCr_xO_y + nH_2 \rightarrow ZnCr_xO_{y\text{-}n} + H_2O \qquad (1)$$

The Zn K-edge XANES spectrum is simulated by using the FDMNES software developed by Yves Joly [25]. Only atoms within the sphere radius of 6 Å formed by absorbing atoms are considered in the final state calculation.

3. Results

3.1. Zn-XANES spectrum simulation

Our investigation starts from the XANES simulation of several likely $ZnCr_xO_y$ bulk crystals to achieve a basic understanding of how catalyst evolves under reaction conditions. Both the stoichiometric $ZnCr_2O_4$ and nonstoichiometric $ZnCr_xO_y$ ($Zn_5Cr_7O_{16}$ and $Zn_3Cr_3O_8$) spinel phases are simulated with the bulk crystal structure obtained from our previous work [6].

Fig. 1b illustrates the simulated Zn K-edge XANES spectra of three $ZnCr_xO_y$ phases. The **A** and **B** peaks appear at 9660–9670 and 9680–9690 eV, respectively. With the decrease of Zn:Cr ratio from 1:1 to 1:2, the peak A shifts to the higher energy accompanied by the intensity decrease while the intensity of peak **B** increases. This reproduces the variations observed in the experimental XANES spectra for both fresh and used $ZnCr_xO_y$ catalysts after the 1000 h catalyst testing (Fig. 1a). It implies the presence of these nonstoichiometric $Zn_5Cr_7O_{16}$ and $Zn_3Cr_3O_8$ phases in the fresh $ZnCr_xO_y$ catalyst and the phase transition to $ZnCr_2O_4$ phase after a long-time reaction. Therefore, we choose the $Zn_3Cr_3O_8$ crystalline phase as the model for investigating the SDR mechanism, which has the maximum $[ZnO_6]$ concentration[6] for the nonstoichiometric $ZnCr_xO_y$ spinel phase.

3.2. Thermodynamics and kinetics of anion and cation migration during SDR

Starting from the most stable $Zn_3Cr_3O_8$ (0001) surface,[6] we investigated the key steps of $ZnCr_xO_y$ SDR by focusing on the migration of O anion and Zn/Cr cations. The $Zn_3Cr_3O_8$ (0001) surface features the unique $[ZnO_6]$ structure pattern in subsurface layer, which switches to the $[CrO_6]$ in the most stable $ZnCr_2O_4$ (1 1 1) surface, see Fig. 1c and Supporting Information (SI) Fig. S1. A number of likely pathways for the anion and cation migrations have been explored by using the SSW-NN method and the most energetically favored pathways are shown in Fig. 2. Others can be found in SI Figs. S2 and S3.

Fig. 2a depicts the Gibbs free energy profiles of the migration of surface and subsurface O atoms. The animation of the pathway can better describe the complex process and included in SI Movie 1. Starting from the perfect $Zn_3Cr_3O_8$ (0001) surface, two surface O atoms can be readily removed by reacting with H_2 sequentially, which releases the energy of 0.44 and 0.36 eV. The resulted two O_vs are separated by a surface O[1] atom (state ***i*** in Fig. 2a). This surface O[1] atom can migrate to fill one of the O_vs with a migration barrier of 1.10 eV (state ***ii*** in Fig. 2a). Subsequently, the subsurface O[2] can move to the surface to

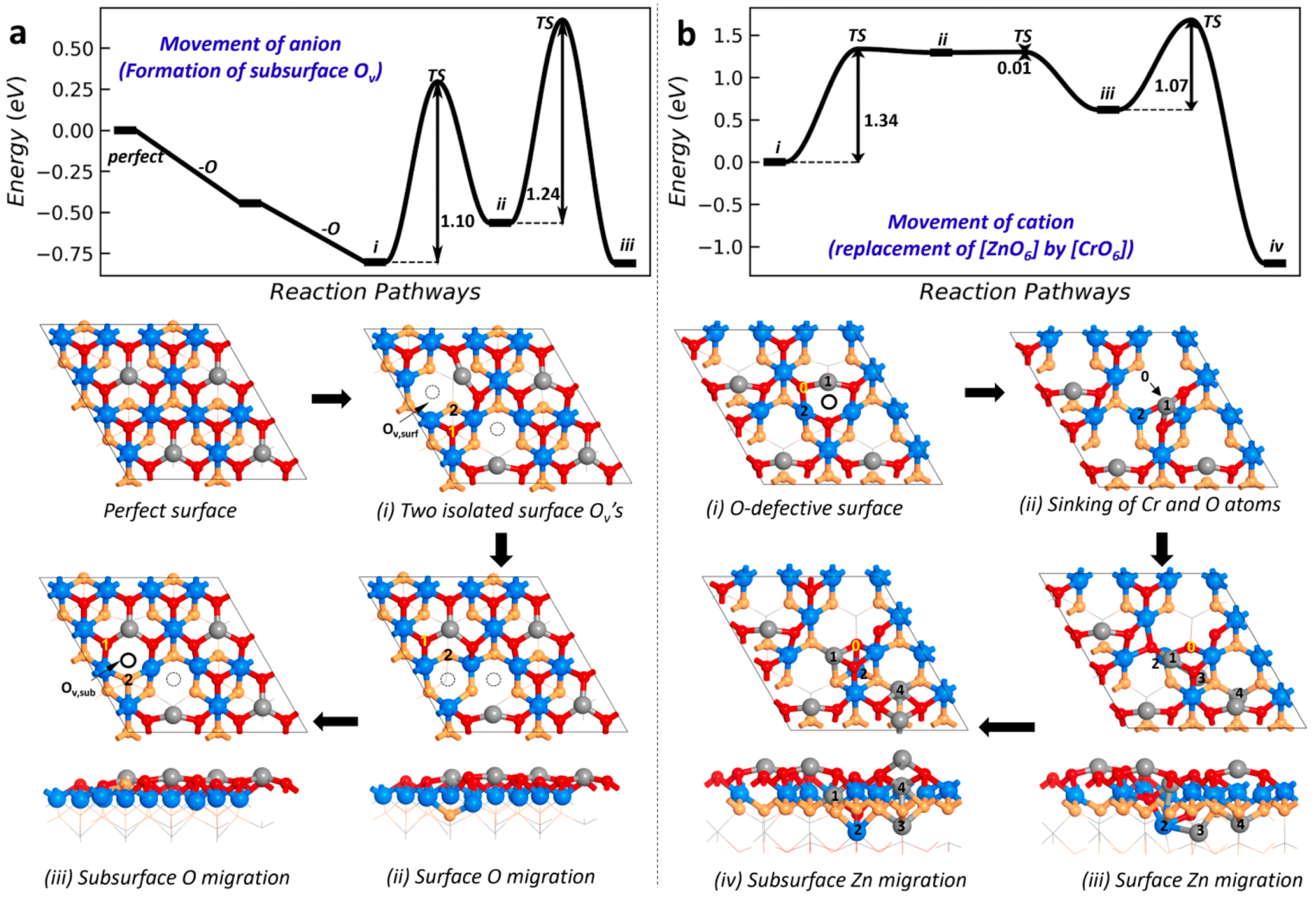

Fig. 2. Gibbs free energy profile of movements of anion and cations at 673 K and 2.5 MPa syngas pressure, i.e. (a) the surface and subsurface O migration to form subsurface O_v and (b) the replacement of subsurface $[ZnO_6]$ by surface $[CrO_6]$. The reaction snapshots are also shown in the figure.

occupy the surface O_v, forming the subsurface O_v (state ***iii*** in Fig. 2a). The formation of subsurface O_v leads to the generation of planar $[CrO_4]_{pla}$ structural unit, identified previously as the key catalytic active site for syngas-to-methanol conversion.[6] The subsurface O migration requires to overcome an energy barrier of 1.24 eV, which becomes feasible under reaction conditions (>600 K). It suggests that the anion movement and thus the dynamics of O_v are common events during syngas conversion.

From the thermodynamics of O_v formation, the surface and subsurface O_v concentration on the $Zn_3Cr_3O_8$ (0001) surface can finally reach to 0.25 monolayer (ML, with respect to all O atoms at the same layer), as already revealed by our previous work.[6] By further performing SSW-NN simulations, we found that the presence of subsurface O_v opens the channel for the cation migration. The cation migration channels are therefore exhaustively explored by using SSW-NN pathway search on the O-defective $Zn_3Cr_3O_8$ (0001) surface with the O_v concentrations of 0.25 ML on both surface and subsurface. The most favorable migration channel relating to Cr migration is thus identified, where the subsurface $[ZnO_6]$ is replaced by surface $[CrO_6]$ via the collective moment of surface/subsurface atoms near a subsurface O_v, as plotted in Fig. 2b. The animation of the pathway can be found in SI Movie 2.

To start the Cr migration, the surface O[0] and Cr[2] ($[CrO_4]_{pla}$) atoms nearby the subsurface O_v sink to the subsurface, where O[0] and Cr[2] atoms move towards the subsurface O_v and the neighboring subsurface $[ZnO_6]$, respectively (state ***i*** to ***ii*** in Fig. 2b). The reaction has a free energy barrier of 1.33 eV and is endothermic by 1.29 eV. Meanwhile, the surface Zn[1] atom moves towards the position initially occupied by Cr[2] atom with the energy release of 0.68 eV and a small energy barrier of 0.01 eV (state ***ii*** to ***iii*** in Fig. 2b). Next, the Cr[2] atom occupies the subsurface octahedral center and squeezes out the original Zn[3] atom ($[ZnO_6]$). The Zn[3] atom moves towards the subsurface $[ZnO_4]$ to occupy the tetrahedral center by pushing the Zn[4] into the $[CrO_6]$ vacancy at the surface layer. This process needs to overcome 1.07 eV energy barriers and strongly exothermic by 1.82 eV. It finally fulfills the replacement of subsurface $[ZnO_6]$ by surface $[CrO_6]$.

Briefly, the exchange between subsurface $[ZnO_6]$ and surface $[CrO_6]$ involves a series of cation positions exchange, starting with Zn[1] and ending with Zn[4], with Cr[2] and Zn[3] involved, i.e., Zn[1] -> Cr[2] -> Zn[3] -> Zn[4]. These exchanges ultimately result in the disappearance of $[ZnO_6]$, the increase of subsurface Cr concentration and the increase of surface Zn:Cr ratio. More importantly, the first step of the replacement of subsurface Zn by surface Cr is the sink of the $[CrO_4]_{pla}$ site into the subsurface layer, causing the disappearance of $[CrO_4]_{pla}$ catalytic active site — the origin for the activity drop.

The replacement of $[ZnO_6]$ by $[CrO_6]$ is identified as the rate-determining step of SDR with the energy barrier of 1.69 eV, corresponding to the reaction rate of $0.01 \sim 2\ s^{-1}$ at typical syngas conversion conditions (573 ∼ 673 K). To compare with experimental data, we estimate the experimental catalyst degradation barrier as follows. Based on the experimental data that the selectivity of syngas-to-alcohol decreases over time from 80 wt% to 60 wt% after 1000 hours[4] and the methanol yield is approximately 200 $g\ kg_{cat}^{-1}h^{-1}$ at 673 K,[5] the catalyst deactivation rate is therefore approximately 0.04 $g\ kg_{cat}^{-1}h^{-1}$ with the ratio of deactivation rate to reaction rate of approximately 1:10000. This information, along with the apparent experimental activation energy for syngas-to-methanol of ∼ 1.20 eV (113 ± 5 kJ mol^{-1}),[9] allows for the estimation of the SDR energy barrier of 1.73 eV (see SI method). Therefore, the experimental barrier is well consistent with our theoretical results.

3.3. *SDR from MD-NN simulation*

To further observe the temperature-dependence of the SDR, we performed long-time MD simulations based on G-NN potential. Our simulation utilizes a large (4 × 6) $Zn_3Cr_3O_8$ (0001) surface consisting of 936 atoms at the O_v concentration of 0.25 ML on both the surface and subsurface layers. There are 24 $[ZnO_4]$ and 72 $[CrO_6]$ structure units in surface layer and 24 $[ZnO_6]$ and 48 $[ZnO_4]$ structure units in subsurface layer in this super cell. MD simulations are carried out at 673, 873 and 1073 K with three trajectories for each temperature and 2 ns for each trajectory.

Fig. 3 illustrates the MD-NN results under different temperatures. At 673 K, the system potential energy fluctuates in a small window — the average potential energy change is < 0.1 eV per 1 × 1 surface after 2 ns (Fig. 3a). Consistently, no obvious subsurface structural reconstruction is observed as reflected by the same number of subsurface $[ZnO_6]$ of 24 and the zero subsurface Cr concentration (divided by the total surface metal atoms per supercell, i.e. 72 atoms), see Fig. 3b and c. The major structural variation occurs at the surface region, where the surface O_vs and Zn atoms tend to agglomerate together, resulting in the formation of a Zn-O-Zn structure pattern and the larger surface cavity (containing more than two O_vs, see Fig. S4).

At 873 K, the system average potential energy decreases by 0.3 eV per 1 × 1 surface after 2 ns, which is larger than that at 673 K. The Cr migration into the subsurface starts at this temperature. In a 2 ns trajectory, the subsurface Cr concentration increases to 0.01 ML, accompanied with 1 ∼ 2 subsurface Zn atoms appearance on the surface (Fig. S5). When the temperature increases to 1073 K, the system's average potential energy dramatically decreases by ∼ 1.0 eV per 1 × 1 surface after 2 ns. The surface Cr atoms enter the subsurface layer as early as the first 0.2 ns, and then the subsurface Cr concentration rapidly increases to 0.175 ML after 2 ns (Fig. 3b and c). We notice that the number of $[CrO_4]_{pla}$ catalytic active site dramatically decreases from 48 to 35, 14 and 11 after 2 ns MD simulation at 673, 873 and 1073 K, respectively. The decrease in the amount of $[CrO_4]_{pla}$ catalytic active site points directly to a decreased catalytic activity with time.

The MD trajectories of subsurface Zn and surface Cr atoms exhibit distinct features. As illustrated in Fig. 3d, the color depth indicates their time of appearance during MD simulation. The Cr atoms display a lighter coloration on surface but a darker coloration on subsurface. Conversely, the coloration of Zn is lighter on the subsurface and darker on the surface. It indicates the migration of Cr from surface to subsurface but the Zn from subsurface to surface. Moreover, the Cr coloration on surface is obviously lighter than the Zn coloration on subsurface, indicating that the surface Cr migration occurs before the subsurface Zn migration.

To further analyze the structural change of the subsurface layer, we examine the radial distribution function (RDF) of the subsurface Zn_{sub}-Zn_{sub} pair before and after MD simulation at 1073 K, as illustrated in Fig. 3e. The RDF shows the probability of finding a Zn atom at a certain distance from another Zn atom in the subsurface layer. The insert figure in Fig. 3e shows the crystal structure of subsurface layer, where the distances of $[ZnO_4]$-$[ZnO_4]$/$[ZnO_6]$ in the first nearest neighbor (red), $[ZnO_6]$-$[ZnO_6]$ in the first nearest neighbor and $[ZnO_4]$-$[ZnO_4]$ in the second nearest neighbor (blue), and $[ZnO_6]$-$[ZnO_4]$ in the second nearest neighbor (green) are ∼ 3.2, 6.0 and 7.0 Å, respectively. These can be identified in the RDF as the first, second, and third peaks at around 3.5, 6, and 7 Å, respectively. After 2 ns, the peak position does not shift, indicating that there is no structural distortion in the subsurface layer and the relative positions of $[ZnO_{4/6}]$ structural units maintain well. However, the intensity of all peaks significantly decreases, particularly, the first peak decreases by almost half. This reduction in intensity is consistent with the reduction of subsurface $[ZnO_6]$ structure units after MD simulations.

3.4. *Slowing down SDR via addition of other elements*

Our SDR mechanism shows that the initial step of Zn/Cr cation migration is the presence of the subsurface O_v which provides the space for the sinking of surface Cr atom. It is thus expected that the inhibition of the subsurface O_v formation should slow down the $ZnCr_xO_y$ SDR. We thus propose to add/dope other elements for adjusting the formation energy of O_v. In principle, the dopant should not stop the catalytic

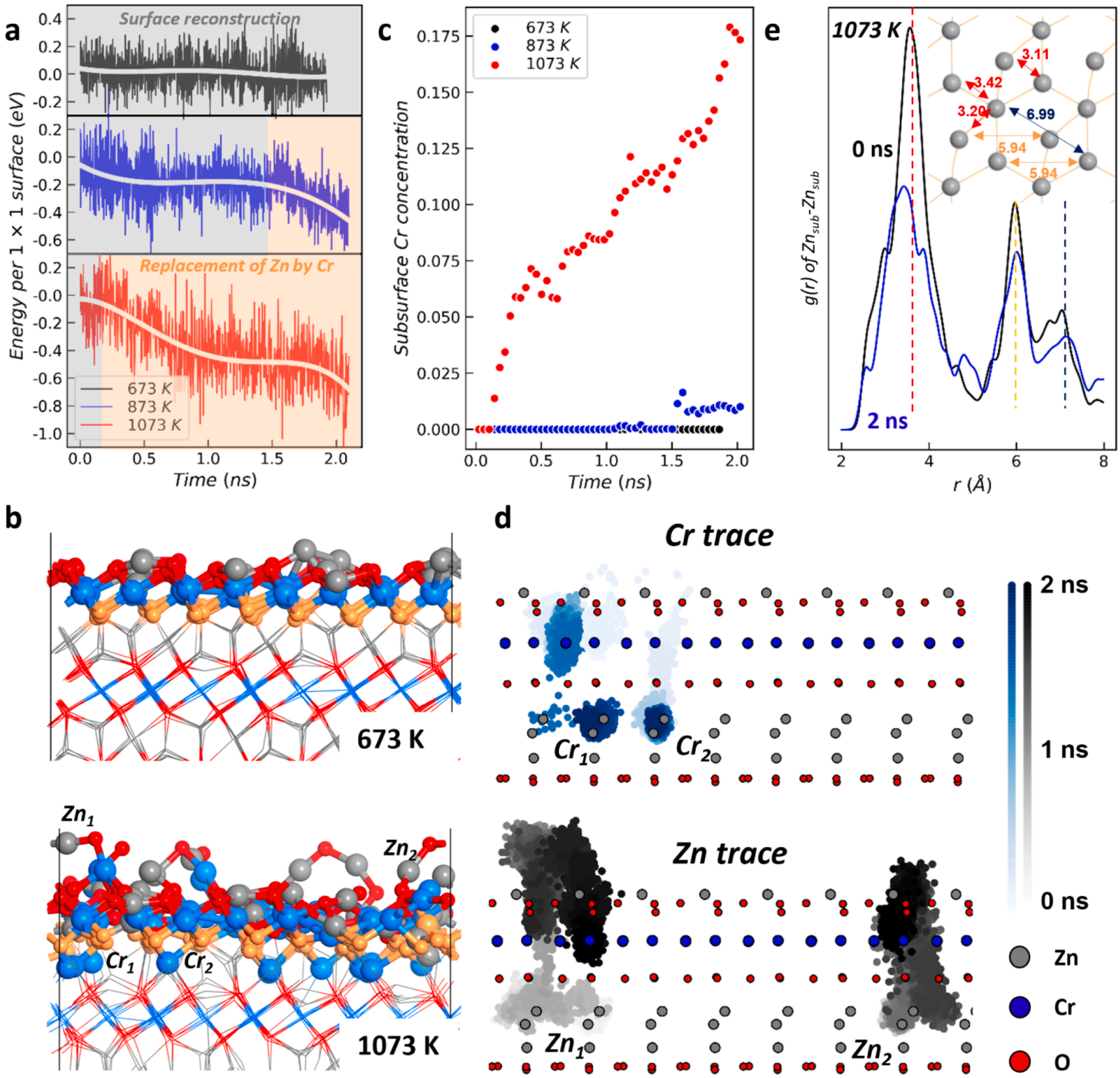

Fig. 3. The MD-NN simulation results of O-defective $Zn_3Cr_3O_8$ (0001) surface with the initial O_v concentrations of 0.25 ML on both the surface and subsurface layers. (a) The energy variations against the MD simulation time at different temperature. (b) The structure after 2 ns MD simulation at 673 and 1073 K. (c, e) The variations of the (c) surface Cr concentration and (e) radial distribution function *g(r)* of subsurface $Zn_{sub} - Zn_{sub}$ pairs against the MD simulation time at 1073 K. (d) MD traces of surface Cr and subsurface Zn atoms at 1073 K. The color depth indicates the time of appearance.

conversion that requires the presence of surface O_v to expose the active site and need to prevent the formation of subsurface O_v. Therefore, a successful dopant must satisfy two quantitative conditions: **(i)** the surface O_v formation free energy $\Delta G_{Ov,\mathrm{surf}} < 0$ eV and **(ii)** the subsurface O_v formation energy $\Delta G_{Ov,\mathrm{sub}} > 0$. Note that, for active catalysts, the presence of subsurface O_v is still required for creating $[CrO_4]_{pla}$ active sites, and thus ideally $\Delta G_{Ov,\mathrm{sub}}$ should be positive but not too positive. The Gibbs free formation energy of surface and subsurface O_vs can be computed using Eq. (1) with the reactant H_2 as the reductant at 673 K and 2.5 MPa syngas pressure with H_2:CO = 2:1 (the typical syngas conversion condition).

By replacing a surface Cr atom with 12 different metal dopants (in 3*d* transitional group and main group III) on $Zn_3Cr_3O_8$ (0001) surface, we have quickly evaluated $\Delta G_{Ov,\mathrm{surf}}$ and $\Delta G_{Ov,\mathrm{sub}}$ for these metal dopants and the results are shown in Fig. 4a. The formation of O_v is much easier with the increase of atomic number from Ti to Zn and Al to In. Among, all the dopants meet the condition **(i)** with the negative $\Delta G_{Ov,\mathrm{surf}}$ but only Ti and Al meet the condition **(ii)** with the positive $\Delta G_{Ov,\mathrm{sub}}$. Comparing with Ti, the Al-doping has a more positive $\Delta G_{Ov,\mathrm{sub}}$ (+0.23 eV), suggesting its higher capability in inhibiting the formation of subsurface O_v.

To further confirm the role of Al dopant in modifying the behavior of $ZnCr_xO_y$ catalyst, we performed a high-temperature MD simulation at 1073 K on the Al-doped (4 × 6) $Zn_3Cr_3O_8$ (0001) surface with an initial O_v concentration of 0.25 ML on both the surface and subsurface layers. A low Al concentration 3% ML on surface is utilized to probe its effects on catalyst SDR. The MD trajectories are analyzed and compared to those of the undoped $ZnCr_xO_y$ catalyst (Fig. 4b).

We found that in the presence of Al the SDR still occurs featuring the Zn/Cr exchange, which may not be surprising as the Al addition is at a low limit (3% ML on surface). More importantly, the Zn/Cr exchange on the Al-doped catalyst has a much less extent. Fig. 4c compares the subsurface Cr concentration with and without Al-doping along the MD

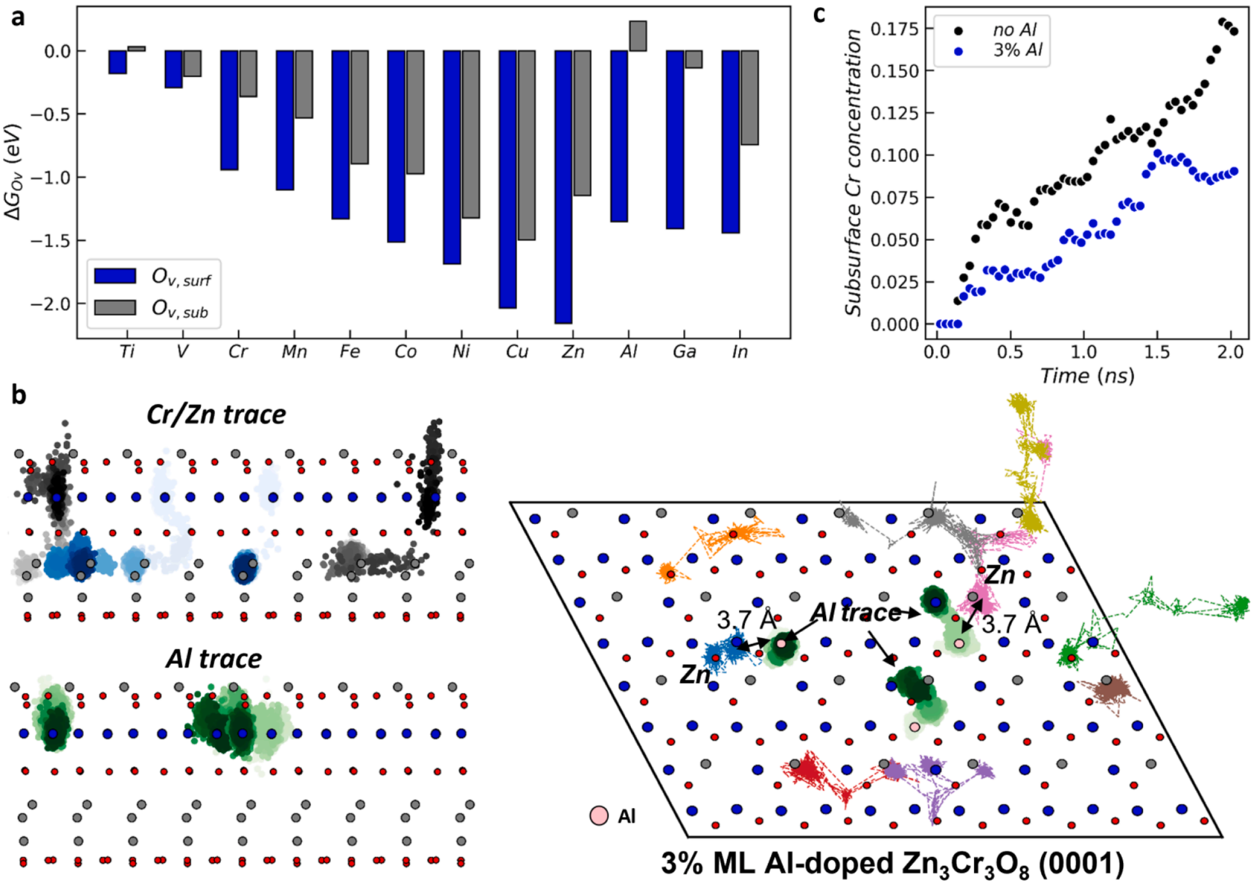

Fig. 4. (a) The Gibbs free formation energy of surface and subsurface O_vs with different metal dopants on $Zn_3Cr_3O_8$ (0001) surface. (b, c) The traces of Al, Cr and Zn atoms and the variations of subsurface Cr concentration during MD simulation for the Al-doped $Zn_3Cr_3O_8$ (0001) surface with the 0.25 ML O_v concentrations on both the surface and subsurface layers at 1073 K. The purple ball represents the Al atoms.

trajectory. After 2 ns, only 0.09 ML Cr atoms migrates from surface to subsurface with Al-doping, which is about half of that without Al-doping (0.18 ML Cr atoms). It is noted that the MD simulation is performed at 1073 K, which is much higher than the typical experimental 673 K. This leads to the higher mobility of Cr to allow the observation in nanoseconds MD simulation. In the experimental temperature, we expect the migration speed will be slowed by 10^{-4} times.

This reduction in SDR can be attributed to the immobility of Al at high temperatures. As above-mentioned, a key event of SDR is the sinking of surface Cr (octahedral site) cations to squeeze out subsurface Zn. The MD trajectories of Al in Fig. 4b (green circle) show that the surface Al atoms (at the octahedral site) only migrate in a small range of surface layer, not sinking into the subsurface layer, indicating that the subsurface $[ZnO_6]$ near Al should not migrate to the surface. Indeed, in our MD trajectory shown in Fig. 4b, there are only two migrated Zn atoms that are close to Al (3.7 Å distance) and the Zn surfacing direction is away from Al. The other migrated Zn atoms are located much distal from the Al atoms. These results further underline the role of Al in modifying the structural properties of $ZnCr_xO_y$ catalysts and improving their stability during catalytic reactions. It can be conceived that when Al element is added with a suitable concentration and distributed evenly into lattice, the catalyst can be maximally stabilized and at the same time maintain the catalytic ability of $[CrO4]_{pla}$ local structure.

4. Discussion

Our SDR mechanism confirms that the $[CrO4]_{pla}$ model proposed in our previous work[6] is the catalytic active site responsible for syngas conversion to methanol. The simultaneous presence of surface and subsurface O_v leads to the formation of $[CrO4]_{pla}$ site. During the SDR process, this Cr active site sinks to the subsurface and squeezes the subsurface Zn out to the surface step-by-step, and as a result the number of $[CrO4]_{pla}$ sites is reduced. This reduction in active sites is consistent with the observed decrease in catalytic activity. Our findings also suggest that the other proposed active site models, including the reduced $ZnCr_2O_4$ surface for syngas-to-ketone [26–27], ZnO surface and ZnO/$ZnCr_xO_y$ interface sites,[13] are not likely for syngas-to-methanol. Since SDR would result in the formation of more $ZnCr_2O_4$ and ZnO active site, the SDR will produce more active sites in these models, contrary to experimental observations. It is interesting to note that the $ZnCrO_x$ catalyst were also reported to have good activity for isobutanol production under 400 °C and 10 MPa [4,11], but the real active site for chain-growth reaction does not been explored in theory due to the complexity of the reaction network.

To enhance the stability of $ZnCr_xO_y$ catalyst at high temperatures, several elements have been added and tested for catalytic activity [28]. Notably, the addition of Al has been found to improve catalytic activity and stability [28–30]. The ZnCrAlO-SAPO34 catalyst with a Zn:Cr:Al ratio near 2:1:1 have demonstrated stable performance with a constant CO conversion of 19% after 100 h at 673 K.[3] The $C_2 - C_4$ olefins selectivity on $ZnCr_xO_y$ catalyst maintains at ~ 27% with the Al-doping but decreases ~ 7% without Al doping after 140 h [28]. XRD analysis of these catalysts does not reveal the presence of Al_2O_3 peaks but instead exhibits the widening of $ZnCr_xO_y$ peaks, indicating that Al may occupy interstitial sites in the spinel skeleton, forming the $ZnCrAlO_x$ multi-element spinel phase [31]. Although XANES spectra have demonstrated that Al presence suppresses the formation of ZnO for $ZnCr_xO_y$ catalysts after 140 h syngas conversion [28], the mechanism for Al stabilization of the catalyst remains unclear. Our results suggest that Al can replace Cr in the octahedral site of the spinel lattice, which inhibits for formation of subsurface O_v and the migration of neighboring Zn/Cr cations. The Al doping, however, inhibits simultaneously the formation of subsurface O_v, leading the disappearance of $[CrO_4]$ active site of methanol synthesis and thus the decrease of reaction activity, as observed in experiments [30]. Apparently, there is a tradeoff between activity and stability. Therefore, an optimal concentration of Al addition in the experimental catalyst (25% Al in $ZnAlCrO_x$) can be understood as a requirement for the homogeneous distribution of Al in the octahedral site of spinel lattice, where each Zn/Cr can have relatively shortest contact with Al and at the meantime maintain the ability to form $[CrO_4]_{pla}$ locally.

5. Conclusion

By using G-NN-based global optimization and long-time MD simulations, this work elucidates the mechanism of nonstoichiometric $ZnCr_xO_y$ SDR. The process begins with surface reconstruction under the reductive reaction conditions, where both surface and subsurface O_v forms and the generation of $[CrO_4]_{pla}$ active site for syngas conversion. The presence of subsurface O_v allows for the subsequent cation migration. The surface Cr cation sinks to the subsurface and squeezes the subsurface Zn out to the surface step-by-step, leading to the replacement of subsurface Zn by surface Cr and the diminishing of the surface $[CrO_4]_{pla}$ active site for syngas conversion. The SDR is driven by thermodynamics towards the more stable stochiometric $ZnCr_2O_4$ and allowed by the kinetics, $\sim$ 1.7 eV. Our results indicate that, paradoxically, the $[CrO_4]_{pla}$ active site generation with the presence of subsurface O_v is also the cause of the catalyst deactivation. By screening 12 different metal dopants, we identify Al-dopant can inhibit the formation of subsurface O_v and slow down the Zn-Cr replacement. These findings may contribute to the development of more efficient and stable catalysts for various industrial applications.

Declaration of Competing Interest

The authors declare that they have no known competing financial interests or personal relationships that could have appeared to influence the work reported in this paper.

Data availability

Data will be made available on request.

Acknowledgment

This work was supported by the National Science Foundation of China (12188101, 22033003 and 22203101), Youth Innovation Promotion Association CAS (No. 2023265) and Science & Technology Commission of Shanghai Municipality (23ZR1476100) and the Tencent Foundation for XPLORER PRIZE.

Appendix A. Supplementary material

The Supporting Information is available free of charge on the ACS Publications website to this article can be found online at https://doi.org/10.1016/j.jcat.2023.07.024.

References

[1] A. Mittasch, M. Pier, K. Winkle, U.S. Patent No. US1558559, 1925.
[2] M.C. Molstad, B.F. Dodge, Zinc Oxide-Chromium Oxide Catalysts for Methanol Synthesis, Ind. Eng. Chem. 27 (2) (1935) 134–140.
[3] F. Jiao, J. Li, X. Pan, J. Xiao, H. Li, H. Ma, M. Wei, Y. Pan, Z. Zhou, M. Li, Selective conversion of syngas to light olefins, Science 351 (6277) (2016) 1065–1068.
[4] S.P. Tian, Y.Q. Wu, H.P. Ren, H.J. Xie, Y.Z. Zhao, Q. Ma, Z.C. Miao, Y.S. Tan, Insights into the deactivation mechanism of Zn-Cr binary catalyst for isobutanol synthesis via syngas, Fuel Process. Technol. 193 (2019) 53–62.
[5] G. Del Piero, F. Trifiro, A. Vaccari, Non-stoicheiometric Zn–Cr spinel as active phase in the catalytic synthesis of methanol, J. Chem. Soc., Chem. Commun. 10 (10) (1984) 656–658.
[6] S. Ma, S.-D. Huang, Z.-P. Liu, Dynamic coordination of cations and catalytic selectivity on zinc–chromium oxide alloys during syngas conversion, Nat. Catal. 2 (8) (2019) 671–677.
[7] M. Bertoldi, B. Fubini, E. Giamello, F. Trifirò, A. Vaccari, Structure and reactivity of zinc–chromium mixed oxides. Part 1.—The role of non-stoichiometry on bulk and surface properties, J. Chem. Soc., Faraday Trans. 84 (5) (1988) 1405-1421.
[8] A. Riva, F. Trifirò, A. Vaccari, L. Mintchev, Structure and reactivity of zinc–chromium mixed oxides. Part 2. —Study of the surface reactivity by temperature-programmed desorption of methanol, J. Chem. Soc., Faraday Trans. 84 (5) (1988) 1423–1435.
[9] E. Errani, F. Trifiro, A. Vaccari, M. Richter, G. Del Piero, Structure and reactivity of Zn-Cr mixed oxides. Role of non-stoichiometry in the catalytic synthesis of methanol, Catal. Lett. 3 (1) (1989) 65–72.
[10] E. Giamello, B. Fubini, M. Bertoldi, A. Vaccari, Structure and reactivity of zinc–chromium mixed oxides. Part 3.—The surface interaction with carbon monoxide, J. Chem. Soc., Faraday Trans. 85 (2) (1989) 237-249.
[11] L. Tan, G. Yang, Y. Yoneyama, Y. Kou, Y. Tan, T. Vitidsant, N. Tsubaki, Iso-butanol direct synthesis from syngas over the alkali metals modified Cr/ZnO catalysts, Appl. Catal. A 505 (2015) 141–149.
[12] S. Tian, S. Wang, Y. Wu, J. Gao, P. Wang, H. Xie, G. Yang, Y. Han, Y. Tan, The role of potassium promoter in isobutanol synthesis over Zn–Cr based catalysts, Catal. Sci. Technol. 6 (12) (2016) 4105–4115.
[13] H. Song, D. Laudenschleger, J.J. Carey, H. Ruland, M. Nolan, M. Muhler, Spinel-Structured ZnCr2O4 with Excess Zn Is the Active ZnO/Cr2O3 Catalyst for High-Temperature Methanol Synthesis, ACS Catal. 7 (11) (2017) 7610–7622.
[14] Y.-F. Li, S.-C. Zhu, Z.-P. Liu, Reaction Network of Layer-to-Tunnel Transition of MnO2, J. Am. Chem. Soc. 138 (16) (2016) 5371–5379.
[15] S.-C. Zhu, S.-H. Xie, Z.-P. Liu, Nature of rutile nuclei in anatase-to-rutile phase transition, J. Am. Chem. Soc. 137 (35) (2015) 11532–11539.
[16] S. Ma, C. Shang, Z.-P. Liu, Heterogeneous catalysis from structure to activity via SSW-NN method, J. Chem. Phys. 151 (5) (2019), 050901.
[17] S. Ma, Z.-P. Liu, Zeolite-confined subnanometric PtSn mimicking mortise-and-tenon joinery for catalytic propane dehydrogenation, Nat. Commun. 13 (1) (2022) 1–8.
[18] S.D. Huang, C. Shang, P.L. Kang, X.J. Zhang, Z.P. Liu, LASP: Fast global potential energy surface exploration, WIREs Comput. Mol. Sci. (2019) e1415.
[19] C. Shang, Z.-P. Liu, Stochastic surface walking method for structure prediction and pathway searching, J. Chem. Theo. Comput. 9 (3) (2013) 1838–1845.
[20] P.E. Blöchl, Projector augmented-wave method, Phys. Rev. B: Condens. Matter Mater. Phys. 50 (24) (1994) 17953–17979.
[21] G. Kresse, D. Joubert, From ultrasoft pseudopotentials to the projector augmented-wave method, Phys. Rev. B: Condens. Matter Mater. Phys. 59 (3) (1999) 1758–1775.
[22] J.P. Perdew, K. Burke, M. Ernzerhof, Generalized gradient approximation made simple, Phys. Rev. Lett. 77 (18) (1996) 3865.
[23] X.-J. Zhang, C. Shang, Z.-P. Liu, Double-ended surface walking method for pathway building and transition state location of complex reactions, J. Chem. Theo. Comput. 9 (12) (2013) 5745–5753.
[24] X.-J. Zhang, Z.-P. Liu, Variable-Cell Double-Ended Surface Walking Method for Fast Transition State Location of Solid Phase Transitions, J. Chem. Theo. Comput. 11 (10) (2015) 4885–4894.
[25] Y. Joly, X-ray absorption near-edge structure calculations beyond the muffin-tin approximation, Phys. Rev. B 63 (12) (2001), 125120.
[26] Z.Z. Lai, N.L. Sun, J.M. Jin, J.F. Chen, H.F. Wang, P. Hu, Resolving the Intricate Mechanism and Selectivity of Syngas Conversion on Reduced ZnCr2Ox: A Quantitative Study from DFT and Microkinetic Simulations, ACS Catal. 11 (21) (2021) 12977–12988.
[27] X.Y. Fu, J.P. Xiao, Toward Understanding and Simplifying the Reaction Network of Ketene Production on ZnCr2O4 Spinel Catalysts, J. Phys. Chem. C 125 (45) (2021) 24902–24914.
[28] G. Pollefeyt, V.P. Santos, D.F. Yancey, D. Nieskens, A. Kirilin, A. Malek, Direct Conversion of Syngas to Olefins over a Hybrid CrZn Mixed Oxide/SAPO-34 Catalyst: Incorporation of Dopants for Increased Olefin Yield Stability, Ind. Eng. Chem. Res. 61 (46) (2022) 17001–17011.
[29] Y. Huang, W. Qian, H. Ma, H. Zhang, W. Ying, Impact of Zn/Cr Ratio on ZnCrOx-SAPO-34 Bifunctional Catalyst for Direct Conversion of Syngas to Light Olefins, Int. J. Chem. Eng. 12 (10) (2018) 557–563.
[30] T. Kull, T. Wiesmann, A. Wilmsen, M. Purcel, M. Muhler, H. Lohmann, B. Zeidler-Fandrich, U.P. Apfel, Influence of the ZnCrAl Oxide Composition on the Formation of Hydrocarbons from Syngas, Acs Omega 7 (47) (2022) 42994–43005.
[31] X.B. Luan, Z.T. Ren, X.P. Dai, X. Zhang, J.X. Yong, Y. Yang, H.H. Zhao, M.L. Cui, F. Nie, X.L. Huang, Selective Conversion of Syngas into Higher Alcohols via a Reaction-Coupling Strategy on Multifunctional Relay Catalysts, ACS Catal. 10 (4) (2020) 2419–2430.